water

MDPI

Article

Velocity Structure of Density Currents Propagating over Rough Beds

Reza Nasrollahpour [1], Mohamad Hidayat Jamal [2,3,*], Zulhilmi Ismail [2,3], Zulkiflee Ibrahim [2], Mazlin Jumain [2], Mohd Ridza Mohd Haniffah [2] and Daeng Siti Maimunah Ishak [3]

[1] Civil Engineering, Schulich School of Engineering, University of Calgary, 2500 University Drive NW, Calgary, AB T2N 1N4, Canada; reza.nasrollahpour@ucalgary.ca
[2] Water and Environmental Engineering, School of Civil Engineering, Faculty of Engineering, Universiti Teknologi Malaysia, Johor Bahru 81310, Malaysia; zulhilmi@utm.my (Z.I.); zulkfe@utm.my (Z.I.); mazlin@utm.my (M.J.); mridza@utm.my (M.R.M.H.)
[3] Center for Coastal and Ocean Engineering (COEI), Research Institute of Sustainable Environment (RISE), Universiti Teknologi Malaysia, Johor Bahru 81310, Malaysia; maimunah.kl@utm.my
* Correspondence: mhidayat@utm.my

Abstract: In most practical cases, density-driven currents flow over surfaces that are not smooth; however, the effects of bottom roughness on these currents have not been fully understood yet. Hence, this study aims to examine the velocity structure of density currents while propagating over rough beds. To this end, alterations in the vertical velocity profiles within the body of these currents were investigated in the presence of different bottom roughness configurations. Initially, laboratory experiments were carried out for density currents flowing over a smooth surface to provide a baseline for comparison. Thereafter, seven bottom roughness configurations were tested, encompassing both dense and sparse bottom roughness. The bottom roughness consisted of repeated arrays of square cross-section beams covering the full channel width and perpendicular to the flow direction. The primary results indicate that the bottom roughness decelerated the currents and modified the shape of velocity profiles, particularly in the region close to the bed. Additionally, a critical spacing of the roughness elements was detected for which the currents demonstrated the lowest velocities. For the spacings above the critical value, increasing the distance between the roughness elements had little impact on controlling the velocity of these currents. Moreover, using dimensional analysis, equations were developed for estimating the mean velocities of the currents flowing over various configurations of the bottom roughness. The findings of this research could contribute towards better parameterization and improved knowledge of density currents flowing over rough beds. This can lead to a better prediction of the evolution of these currents in many practical cases as well as improved planning and design measures for the control of such currents.

Keywords: density current; velocity profile; acoustic doppler velocimeter; bottom roughness

Citation: Nasrollahpour, R.; Jamal, M.H.; Ismail, Z.; Ibrahim, Z.; Jumain, M.; Mohd Haniffah, M.R.; Ishak, D.S.M. Velocity Structure of Density Currents Propagating over Rough Beds. *Water* **2021**, *13*, 1460. https://doi.org/10.3390/w13111460

Academic Editors: Jochen Aberle and Robert Bose

Received: 23 April 2021
Accepted: 20 May 2021
Published: 23 May 2021

1. Introduction

Density currents are generated when the fluid of one density is released into another fluid with a different density. The density difference can result from temperature gradients, dissolved contents, suspended particles, or a combination of them. A wide range of flows are classified as density currents, and it emphasizes the importance of studying them. The most usual type of these currents is an underflow produced when a flow is introduced into an ambient fluid of a lower density. In oceanic and river systems, these currents occur because some of the water in an estuary, ocean, lake is colder, saltier, or contains more suspended sediment than the surrounding water [1,2]. The density-driven currents are known as the main agent for sediment transport in reservoirs; these can carry incoming suspended sediments and existing sediment deposits over the reservoir bed to the area near the dam. These currents decelerate as they approach the dam, and this can give rise to

sedimentation [3]. Reservoir sedimentation is a worldwide issue hindering the sustainable use of reservoirs and sediment balance of impacted rivers [4]. The loss of storage capacity in dam reservoirs due to sedimentation has been an issue of great concern and a topic of research [5–8].

Details regarding velocity profile and friction coefficients in open channel flows can be found in [9]. In the case of density currents, however, the flow is confined to the bed at the bottom and normally bounded by the stationary ambient fluid at the top. The velocity vanishes at the bed and interface between the current and ambient fluid; thus, the velocity distribution attains a peak (maximum) velocity u_m at a distance h_m above the bed. This forms a boundary between the inner and outer layers of the velocity profiles [10]. As seen in Figure 1, the vertical downstream velocity of density currents is divided into two regions: an inner region below the location of maximum velocity, which has a steep increase in velocity from the bottom to the maximum velocity, and an outer region above the maximum velocity with a negative velocity gradient.

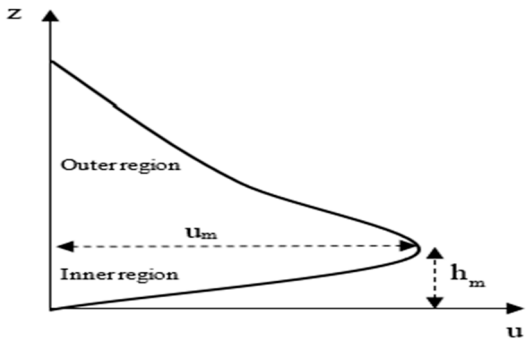

Figure 1. Sketch of a typical vertical velocity profile.

The general approach for density current studies has been simplifying the situation by regarding the bed as smooth [2,11–16]. However, in most practical cases, these currents usually flow over surfaces that are not smooth, such as, mobile beds, obstacles, grain roughness (e.g., sand or gravel), and form roughness (e.g., ripples or dunes). Particularly, there is still a gap in knowledge on the interaction between bottom roughness and the continuous flow of density-driven currents. In studying obstacles for mitigation of density-driven currents, the bulk of literature concerns the case of an isolated (single) roughness element or obstacle, for example [17–20]. There have also been limited investigations in respect to the effect of form roughness on these currents, including Negretti et al. [21], Peters [22], Tanino et al. [23], Tokyay [24], Chowdhury [25], Bhaganagar [26], Howlett et al. [27], Nasrollahpour et al. [28], and Köllner et al. [29]. These works have been mostly focused on the frontal region of the density currents. Overall, the behavior of the continuous flow of density-driven currents over nonplane beds is complex and not fully understood yet, despite its important implications. The interaction of density currents with submarine installations (e.g., porous screens, dykes, oil and gas pipelines, cables) can lead to disastrous damages [30,31]. As an example, a natural turbidity current was captured in the Fraser River delta slope (Canada) that was powerful enough to carry a one-ton observatory platform and severe a heavily armored cable [32].

The bottom roughness can be representative of various scenarios where density currents flow over nonplane surfaces. Additionally, the roughness elements can be a good approximation to submerged dams employed for controlling sediment deposition in reservoirs and to obstacles installed in rivers for retardation of the incoming density currents. Moreover, they can represent obstacles used for partially or entirely stopping density currents transporting pollutants or hazardous materials. Therefore, studying these currents over roughness arrays can have considerable benefits for human and environmental safety purposes and lead to more accurate management of various industrial and natural scenarios.

The main aim of this study is to extend previous studies by considering the effect of bottom roughness on the velocity structure of the density currents. This is achieved through the following specific objectives: (1) to acquire the vertical structure of streamwise velocities within the body of density currents; (2) to investigate alterations in the velocity profiles at the presence of various bed roughness configurations; (3) to develop equations for estimating mean velocities of the currents flowing over various configurations of bottom roughness.

2. Materials and Methods

2.1. Experimental Setup

This study creates density currents in a lock-exchange configuration in which a gate separates two fluids with different densities. To model these currents in the laboratory, a specific setting (illustrated in Figure 2) was employed to prepare dense fluids and maintain the steady state of density currents during each experiment. Prior to each experiment, dense fluids were prepared in the two mixing tanks with a combined volume of 6 m^3 through continuous circulation in a closed-loop system. Furthermore, salt was dissolved in tap water inside the tanks until the required salinity was obtained and the solution was homogeneously mixed; dye was added to the dense fluids during the circulation process for visualization purposes. To prevent fluctuations, a head tank located 3 m above the ground on a steel structure was used to transfer the prepared dense fluids to the flume with a constant head.

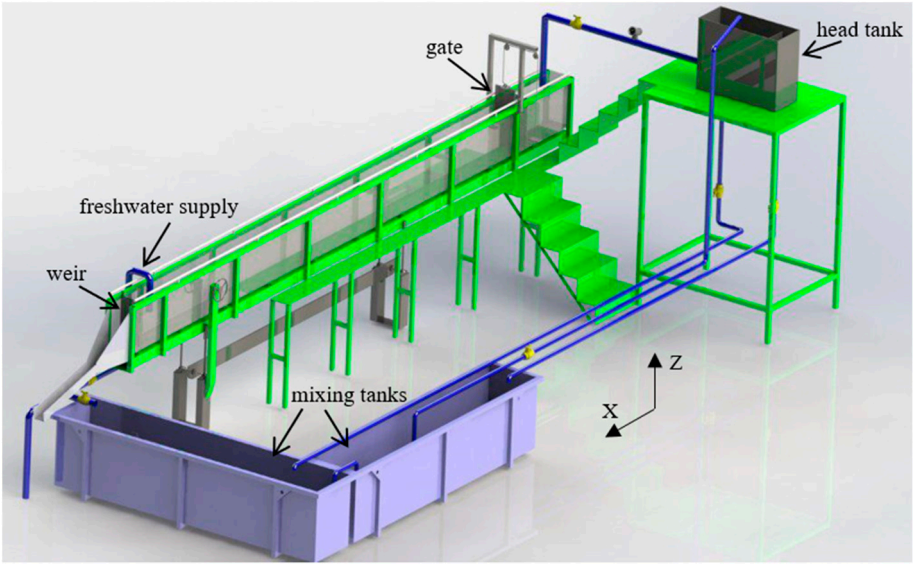

Figure 2. Schematic sketch of the experimental set-up.

The flume was 10 m long, 0.3 m wide, and 0.7 m deep, capable of having different bottom slopes. A sliding vertical gate located at a 1.25 m distance from the upstream end of the flume divided this into two sections of unequal length. Additionally, an overflow weir was at the downstream end of the flume kept the depth of lighter ambient fluid constant during each experiment. The upstream of the gate was occupied by the dense fluid while the downstream part was occupied by freshwater simulating a reservoir where a density current can propagate. The density currents were initiated by the sudden removal of the vertical lock gate. Once the gate was opened, a density current (heavier fluid) advanced through the fresh ambient water (lighter fluid) by a raised front (also known as the head) in the form of an underflow. After the front reached the downstream end of the channel, it was directed for withdrawal. Thereafter, a shallower steady and quasi-uniform layer of density current was formed known as the body (see Figure 3) which is the focus of this study.

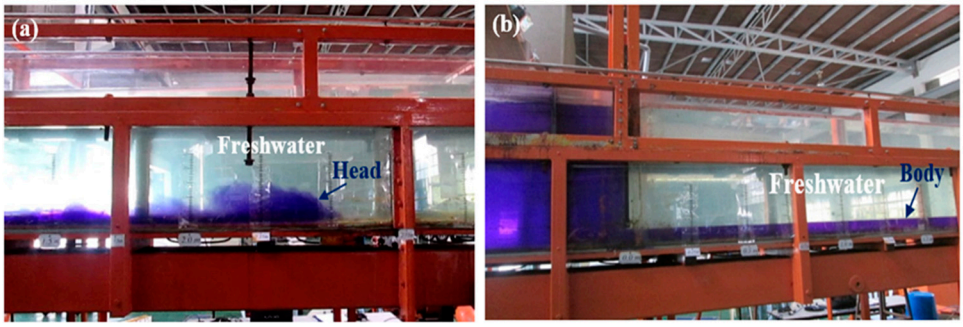

Figure 3. (**a**) Head and (**b**) body of a density current flowing under a layer of stationary ambient freshwater.

2.2. Experimental Measurements

A Vectrino Plus Velocimeter with a lab probe made by Nortek (Akershus, Norway) was used to record the velocity profiles in the body of density currents. This is a high-resolution 10 MHZ Acoustic Doppler Velocimeter (ADV), having a down-looking fixed-stem probe. The ADV has an acoustic sensor consisting of one transmit transducer and four receive transducers, all calibrated by the manufacturer. The receivers are positioned in 90° increments on a circle around the transmitter, slanting 30° from the axis of the transmitter. The sampling volume is the focus point of the receiver beams, situated 5 cm away from the probe to ensure a nearly nonintrusive velocity measurement [33]. The transmitter sends out short acoustic pulse pairs with a known frequency transmitted along the vertical axis, and their echoes are recorded by the receiver arms as the pulses travel through the sampling volume. The echo is reflected from the small particles floating passively in the flow, assuming to have a velocity the same as the flow. The ADV works based on the Doppler principle, meaning the shift between the frequencies of the transmitted pulse and the received echo is proportional to water velocity. The phase shift between two subsequent pulses is then processed to find the actual velocity of the flow.

The body of density currents was maintained by a continuous feed of dense saline fluid moving under a layer of stagnant freshwater. In addition, the discharge rate of dense fluid to the channel was fixed at the desired rate using a flowmeter. The steady condition was considered achieved when recorded velocities at one point in two minutes were the same. The depth of the current at a given station was also checked for remaining unchanged over time to ensure achieving the steady state. Local velocities were then recorded at three locations (i.e., X = 3, 4, and 5 m from the gate) along the centerline of the channel from vertical points above the channel bed. In any required section, the velocity profile was determined by changing the vertical location of the sensor. The measurements began from the top part of the dense layer and continued into the lower parts by lowering the probe into the current till all the necessary points were covered. About 10 points were collected for plotting a vertical profile of velocity at each station; the data recording took about 1 min for each of the measurement points. A sampling frequency of 100 Hz was used, and the samples with signal-to-noise (SNR) values less than 15 dB and correlation less than 70% were filtered according to the manufacturer's recommendation.

Samples were taken from the dense fluids at mixing tanks, head tank, and the region behind the gate to ensure the formation of a homogeneous dense fluid with the desired density. Moreover, at the data collection stations, sampling siphons were used to collect samples from within the currents in the proximity of the bed. To measure conductivity (also known as electrical conductivity EC) of the taken samples, a WP-84 conductivity meter (TPS Pty Ltd., Brendale, QL, Australia) with a K = 10 sensor was employed. Then, mass concentration C (g/L) of the taken samples was derived from its conductivity value EC (millisiemens) utilizing a calibration curve. The calibration curves were yielded by preparing several reference samples of known salt concentration and recording their corresponding conductivity values. Furthermore, a DA-130N Portable Density Meter (Kyoto Electronics Manufacturing, Kyoto, Japan) was used to measure the density φ

(g/cm^3) of the collected samples. Care was taken to obtain dense fluids with approximately the same temperature as those of the clear water in the flume; the maximum temperature difference was 0.5 °C. This ensured that the density differences between dense and ambient fluids were solely due to the salinity differences.

2.3. Experimental Parameters

By definition, roughness elements should not block the flow of density currents [34]. So, this study used bed roughness for which the elements' height fell below the peak velocity position. For the smooth bed experiments, the lowest position of peak velocity occurred at 1.5 cm above the bed. Therefore, the height of the beams was selected as 1.2 cm so that it always fell below the maximum velocity height. The rough beds consisted of arrays of square cross-section beams fabricated from wood with side dimensions of 1.2 cm. The elements spanned full flume width perpendicular to the flow direction, in a repeated array extended over the area downstream of the gate. The desired roughness was obtained by gluing roughness elements on the bed with the required spacing. The diagram of the configurations of the roughness arrays is schematically shown in Figure 4 where λ is the downstream spacing between every two subsequent beams, and Kr is roughness height. One smooth bed and seven roughness configurations (λ/Kr = 1, 4, 8, 16, 32, 64, and 128) were tested herein adopting both dense and sparse bottom roughness elements. According to the classification of [35], λ/Kr = 1 corresponds to the d-type while λ/Kr = 4, 8, 16, 32, 64, and 128 correspond to the k-type bottom roughness.

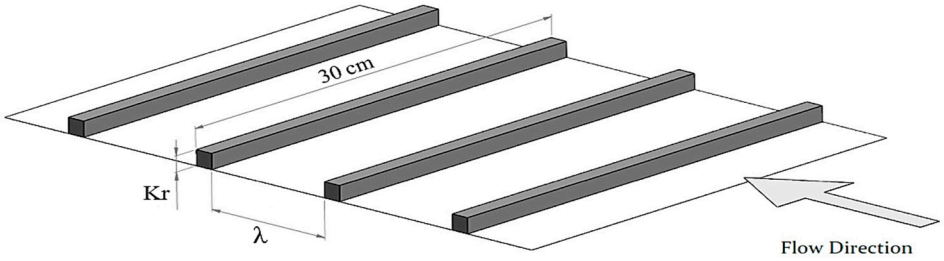

Figure 4. Sketch of the configurations of the roughness arrays.

A total of 64 experiments were performed with different initial parameters listed in Table 1. The creation of density currents with different initial conditions was to ensure repeatability. An inlet gate opening height h_{in} = 7 cm was tested to create subcritical conditions at the inlet. Two bed slopes S = 0.25% and 1.75% were selected based on the experimental circumstances. To create currents with different velocities at the inlet, two discharges of dense fluid Q_{in} = 0.5 and 1 L/s were considered. Additionally, two initial mass concentrations of dense fluids C_{in} = 5 and 15 g/L were chosen to examine currents having different excess densities. These concentrations corresponded to densities of 1.003 and 1.009 gr/cm^3, respectively.

Table 1. Experimental conditions.

Number of Experiments	Roughness Conditions	h_{in} (cm)	S (%)	C_{in} (g/L)	Q_{in} (L/s)
8	Smooth	7	0.25, 1.75	5, 15	0.5, 1
8	λ/Kr = 1	7	0.25, 1.75	5, 15	0.5, 1
8	λ/Kr = 4	7	0.25, 1.75	5, 15	0.5, 1
8	λ/Kr = 8	7	0.25, 1.75	5, 15	0.5, 1
8	λ/Kr = 16	7	0.25, 1.75	5, 15	0.5, 1
8	λ/Kr = 32	7	0.25, 1.75	5, 15	0.5, 1
8	λ/Kr = 64	7	0.25, 1.75	5, 15	0.5, 1
8	λ/Kr = 128	7	0.25, 1.75	5, 15	0.5, 1

To determine the flow regime of density currents, nondimensional numbers were calculated. Like the free surface flow, the driving mechanism of density current is the gravitational force, and the Froude number is considered important. However, gravitational acceleration is reduced due to the density difference, and densimetric Froude number (Fr_{in}) at the inlet is calculated as $Fr_{in} = u_{in}/ (g' h_{in} \cos\theta)$, where u_{in} is the velocity of current at the inlet, g' is reduced gravitational acceleration, h_{in} is the inlet opening height, and θ is bottom slope angle. The reduced gravitational acceleration is $g' = g (\varphi_{in} - \varphi_a)/\varphi_a = g \Delta\varphi/\varphi_a$ where g is the gravitational acceleration, φ_{in} is the initial density of the current, φ_a is the density of the ambient fluid, and $\Delta\varphi$ is the density difference between the current and ambient fluid. Furthermore, the inlet Reynolds number for these currents is defined as $Re_{in} = (u_{in} h_{in})/\nu_{in}$, where u_{in} is inlet velocity, h_{in} is inlet opening height, and ν_{in} is the kinematic viscosity of the dense fluid at the inlet. Due to low concentrations, the inlet dynamic viscosity was set approximately equal to that of the water [36]; therefore, inlet Reynolds number for the flume with width b can be rewritten as $Re_{in} = Q_{in}/b\,\nu$. The inlet Froude number ranged between 0.21 to 0.97; the inlet Reynolds numbers for Q_{in} = 0.5 and 1 L/s were equal to 1956 and 3912, respectively. This indicates that the currents tested in this work were subcritical and turbulent.

The boundary between the density current and ambient fluid is unclear because of the turbulence along the interface. Thus, Ellison and Turner [37] equations are generally recommended to calculate the average velocity ($\overline{u}$) and height ($\overline{h}$) of the density currents:

$$\overline{u} = \frac{\int_o^{h_d} u^2\, dz}{\int_0^{h_d} u\, dz} \quad (1)$$

$$\overline{h} = \frac{\left(\int_0^{h_d} u\, dz\right)^2}{\int_0^{h_d} u^2\, dz} \quad (2)$$

where u is local velocity at depth of z and h_d is the depth where u = 0.

3. Results and Discussion

3.1. Distribution of Velocity

For all the experiments, the velocity profiles were similar but scattered in a specific range. Two different algebraic expressions were used to formulate the velocity distribution in the velocity profiles. One is valid in the rigid boundary (inner or wall region) along the bed, whilst another is valid in the diffusion boundary (outer or jet region). In the wall region, below the maximum velocity ($z < h_m$), the velocity distribution can be represented by an empirical power relation proposed by Altinakar et al. [38]:

$$\frac{u(z)}{u_m} = \left(\frac{z}{h_m}\right)^{\frac{1}{n}} \quad (3)$$

where u(z) is the mean streamwise velocity at the distance z above the bed, u_m is the maximum velocity, h_m is the height where the maximum velocity occurs, and n is an empirical exponent. The u_m and h_m were obtained for all the collected velocity profiles and used to plot the normalized profiles in the wall region; examples of these profiles are shown in Figure 5.

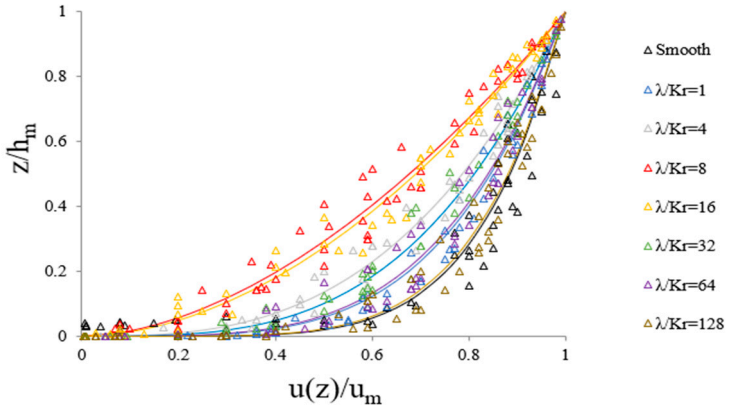

Figure 5. Dimensionless velocity profiles in the wall region at X = 4 m (Note: points are experimental data, and solid lines are fitted profiles).

To determine the constant n, Equation (3) was fitted to all the normalized velocity profiles in the inner region for different bed configurations. The outcomes of the curve fits are listed in Table 2 and compared with those of the literature. Herein, the coefficient of determination (R^2) was used to verify the accuracy of the curve fits; the R^2 values were close to unity showing that the power law well estimated the velocity distribution in the dataset. Given the constant n= 5.61 yielded for the smooth bed tests, the agreement between the results of this study to those of the literature was satisfactory. Note that in Altinakar et al. [38], Nourmohammadi et al. [13], He et al. [39], and Yaghoubi et al. [19] the experiments were performed over a plane bed. Moreover, the inlet Froude numbers for these studies ranged between 1 and 2.33, 0.6 and 3.6, 0.48 and 0.71, and 0.8 and 1.55, respectively, while here this range was between 0.28 and 0.97.

Table 2. Constants obtained for Equations (3) and (4).

Reference	Bed Type	n	R^2	α	m	R^2
[19]	Smooth	6.2	0.95	0.85	2	0.92
[39]	Smooth	5.9	0.97	1.42	2.34	0.97
[13]	Smooth	5.8	—	0.6	2.7	—
[38]	Smooth	6	—	1.4	2	0.96
Present Study	Smooth	5.61	0.92	1.86	2.38	0.91
	λ/Kr = 1	4.28	0.98	1.91	2.63	0.92
	λ/Kr = 4	2.89	0.98	1.33	2.44	0.89
	λ/Kr = 8	1.78	0.97	1.18	2.72	0.90
	λ/Kr = 16	1.87	0.98	1.28	2.54	0.93
	λ/Kr = 32	3.32	0.98	1.68	2.44	0.91
	λ/Kr = 64	3.96	0.96	1.86	2.35	0.89
	λ/Kr = 128	5.45	0.96	1.96	2.39	0.94

As seen in Table 2, the constant n varied from 5.61 for the plane surface to 1.78 for the rough bed with λ/Kr = 8. These variations stemmed from changes in the position of maximum velocity at the collected velocity profiles. Smaller constant n values represent velocity profiles where peak velocities were attained at higher positions. Given the fluctuations in the constant n for different bottom roughness configurations, this can be inferred that the primary controlling parameter in the wall region was the bottom friction.

In the jet region, above the maximum velocity ($z > h_m$), Altinakar et al. [38] suggested a near-Gaussian relation describing the velocity distribution above the maximum velocity point as:

$$\frac{u(z)}{u_m} = \exp\left[-\alpha\left(\frac{z - h_m}{\bar{h} - h_m}\right)^m\right] \quad (4)$$

where u(z) is the mean streamwise velocity at the distance z above the bed, u_m is the maximum velocity, h_m is the height where the maximum velocity occurs, $\bar{h}$ is average current height calculated from Equation (2), α is an empirical constant, and m is an empirical exponent. The u_m, h_m, and $\bar{h}$ were obtained for all of the collected velocity profiles and used to plot the normalized profiles in the jet region; examples of the normalized profiles can be seen in Figure 6. As seen, the scatter of dimensionless velocities in the jet region was more compared to those of the wall region, which is due to the transitory behavior of the currents at their top edge.

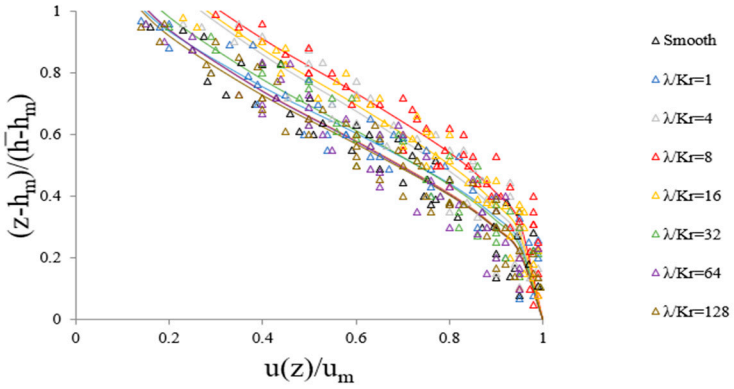

Figure 6. Dimensionless velocity profiles in the jet region at X = 4 m (Note: points are experimental data, and solid lines are fitted profiles).

In the jet region, Equation (4) was fitted to the normalized velocity profiles for the currents over different bed configurations. The computed values of α and m are listed in Table 2 and compared with those of the literature. The results show that the agreement with the literature was rather satisfactory given the experimental difficulties involved. Moreover, the Gaussian law can be used to well-describe the outer region of velocity profiles in this rough bed dataset. Alteration in α and m was minimal indicating that the shape of the outer regions of the normalized velocity profiles did not change substantially with bed types.

3.2. Influence of Roughness on Velocity Profiles

The downstream evolution of velocity profiles is shown in Figure 7, which illustrates changes in the velocity structure of currents in presence of roughness arrays. Herein, the dense layer height (z) and velocity (u) were normalized with the inlet opening height (h_{in}) and inlet velocity (u_{in}), respectively. In general, the velocities decreased as the currents traveled over different bed configurations, and the peak velocities occurred at higher positions above the bed. The driving force of these currents is the density difference between the currents and ambient fluid. The influx of ambient freshwater into the underflows results in reduction of their excess densities, which in turn reduces the velocity of these currents while traveling downstream.

As seen in Figure 7, the changes in the peak velocities and their positions were negligible for the smooth bed, while a stronger deceleration was observed in the case of the rough beds. Additionally, the distance from the bed to the point of maximum velocity shifted further upward for the currents over the rough beds. However, the magnitude of adjustments in the peak velocities and their positions appeared to vary depending on the roughness elements configuration. A comparison of the results reveals that the smallest changes occurred for the currents over the plane surface, which was followed by the currents flowing over the rough beds with λ/Kr = 1 and 128. With increasing the spacing, the peak velocities continued to decrease further till the currents over the spacing of λ/Kr = 8 where the most significant adjustments were observed.

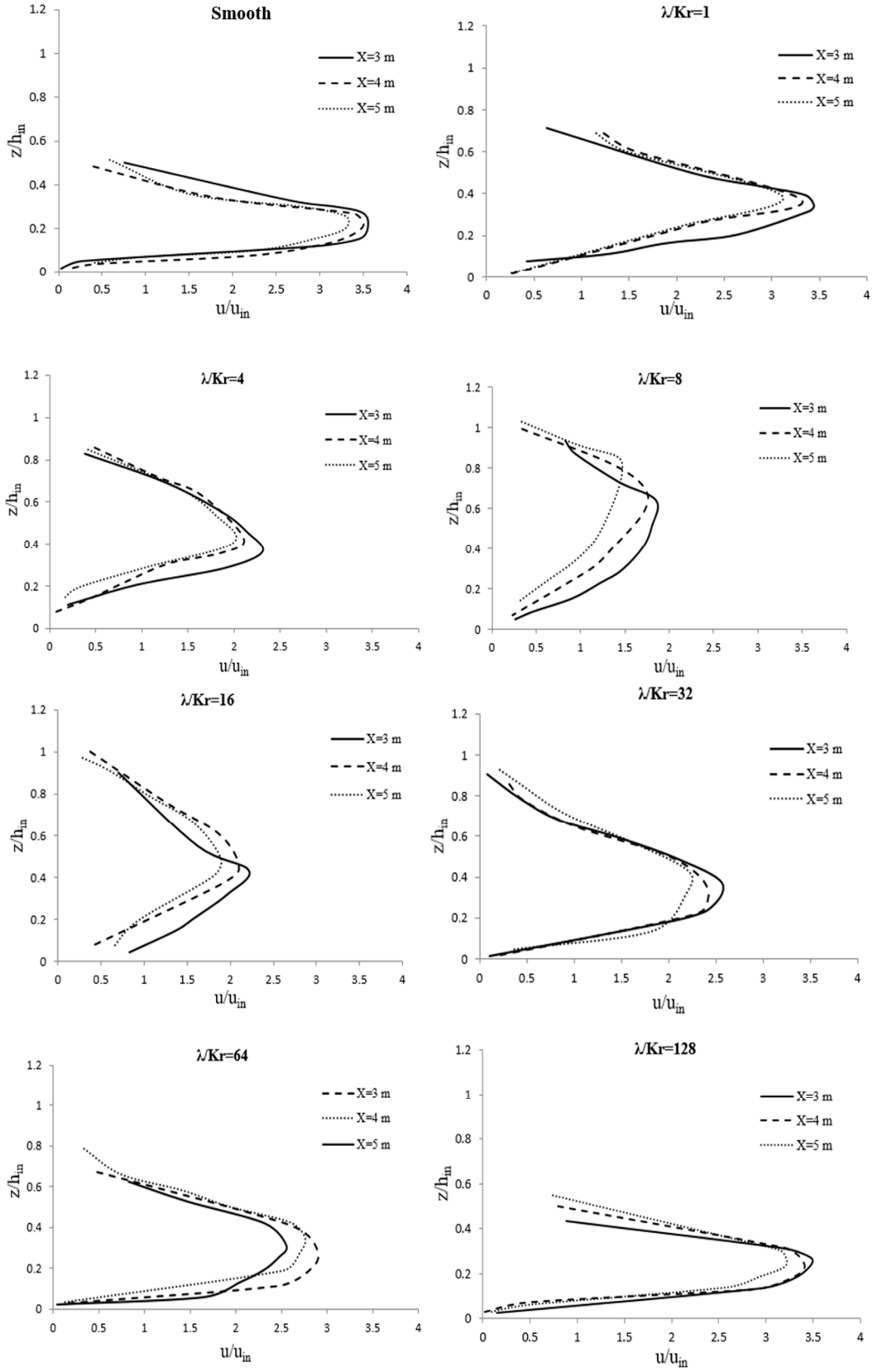

Figure 7. Velocity profiles at different locations for smooth and rough beds corresponding to h_{in} = 7 cm, C_{in} = 15 g/L, Q_{in} = 0.5 L/s, and S = 0.25%.

Following [35], the roughened beds with λ/Kr =1 are categorized as d-type, and the beds with λ/Kr = 4, 8, 16, 32, 64, 128 are considered as k-type. Figure 8 illustrates the influence of different configurations of bottom roughness on the velocity profiles for a selected number of experiments. Note that all these currents had the same initial conditions, and the adjustments in the profiles were solely induced by the bottom roughness. As seen, the primary influence of roughness was decreasing the velocity of the currents. The currents lost their kinetic energy as traveling over the elements due to adverse pressure gradient induced by the inclined upstream surface of the beams, which led to the deceleration of the currents. Also, the velocity maximum for the currents over roughened beds was located higher in comparison with the smooth bed case. However, the magnitude of these effects depended on the configuration of roughness elements, as discussed afterward.

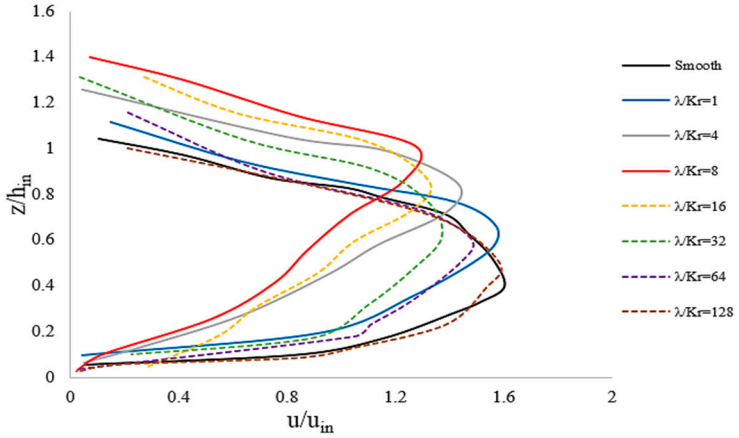

Figure 8. Comparison of velocity profiles for different bed types at X = 4 m corresponding to h_{in} = 7 cm, C_{in} = 5 g/L, S = 1.75%, Q_{in} = 1 L/s.

For the currents over λ/Kr = 1, the velocity profiles depicted close similarity with the smooth bed and noticeably different from other roughened cases. For the rough bed with λ/Kr = 1, the peak velocity was only slightly lower than that of the smooth bed. Nevertheless, the position of peak velocity for this bed type shifted further upward reaching h/h_{in} = 0.65 in Figure 8, as opposed to the corresponding current flowing over the smooth bed where h/h_{in} = 0.4. This suggests that for λ/Kr = 1, the current lifted above the roughness elements. The initial density difference between the ambient water and the dense fluid was small; therefore, the currents flowing over the dense array of beams (λ/Kr = 1) could lift above the beams and showed a dynamic similar to their counterparts traveling over the smooth bed. The front of density currents flowing over d-type roughness was examined by [22,34,40], and a similar mechanism was found in which the head floated over the roughness elements and had only a slight interaction with them. In addition, they reported rotating weak vortices trapped between the elements, which agrees with the findings reported herein.

For the k-type rough beds, two different behaviors were observed in the collected velocity profiles of the currents. As seen in Figure 8, maximum retardation of the currents occurred for the rough surface with the critical spacing of λ/Kr = 8. For the spacing less than the critical value (λ/Kr =4), the retardation of the currents increased with increasing the gaps between elements. For the spacing more than the critical value (λ/Kr = 16, 32, 64, 128), the retardation of the currents diminished with increasing the gap between the elements. For the critical spacing, the currents depicted the smallest velocity maxima and the highest position of velocity maxima. As an example, according to Figure 8, the peak velocity for the current over λ/Kr = 8 decreased by 32.3%, and its height rose by 149.8% compared to the plane bed case.

Flow separation occurs above each beam as the current propagates over the roughness elements. The flow reattaches on the bottom wall in between the beams and separates

again as the next element is approached. This creates a vortex below the separated flow at the downstream side of the beams which ejects to the overlying flow [41,42]. For the spacing between the roughness elements that were large enough, the reattachment length was not affected by the presence of other elements [41,42]; this critical spacing appeared to be $\lambda/Kr = 8$ herein. The critical value represents the spacing in which the maximum strength of ejection occurred, which could have significant effects on the density currents propagation and entrainment. For single-phase flows, the strength of the ejections from between the roughness elements got more till the critical spacing of $\lambda/Kr \approx 7$ was achieved [41,42]. Herein, the evidence was shown that this rule applied to density currents as well.

For the spacing less than the critical value ($\lambda/Kr = 4$), further deceleration of the currents was attributed to the larger spacing between the beams, and the reattachment length was expected to shorten due to adverse pressure gradient induced by the next element. The larger gaps between the beams required more energy to maintain a vortex in motion in that area. Also, the volume of released fluid from between the elements to the current was more significant making more disruption leading to deceleration of the currents. For the rough beds, increasing the spacing between elements increased the distance above the bed where the maximum velocity attains. As observed in the velocity profiles, for the spacing above the critical one (λ/Kr = 16, 32, 64, 128), increasing the distance between the elements had little impact on reducing the velocity of the currents. In other words, increasing the cavities between the beams decreased the retardation of the currents. For $\lambda/Kr = 128$, when the elements were too far apart, the current dynamics reverted to that over a smooth surface with the highly dispersed elements representing very small individual elements in the path of the current. Regarding the spacings more than the critical value, the reattachment length was expected to increase, and the overlying fluid dynamics were once again similar to those encountered above the smooth surface.

3.3. Shear Stress

The measurement of the velocity profiles allowed for a backward calculation of the bottom shear stresses. This study employed the mean flow method to estimate the shear velocities [13,14]. The velocity profiles within the inner region vary logarithmically with depth, and the Von Karman–Prandtl Law of the Wall applies to them as [43]:

$$u = \frac{u^*}{k} \ln \frac{z}{z_0} \tag{5}$$

where u is the velocity at height z above the bed, u* is shear velocity, K = 0.41 is Von Karman constant, and z_0 is zero velocity roughness height. The Equation (5) can be rewritten as:

$$u = \frac{u^*}{k} \ln z - \frac{u^*}{k} \ln z_0 = mx + c \tag{6}$$

As mentioned in Section 2.2, the velocity (u) was collected at several points (z) above the bed within the body of density currents. To determine the distance above the bed in which the logarithmic law was valid, all the data points were used to regress ln(z) versus u. This was observed that the best fit could be achieved at $Z/h_m = 0.88$ with $R^2 = 0.86$. Therefore, only the data points which fell within this distance were used to calculate the shear velocity, and slope (m) of the regression line was used to compute the shear velocity as u* = Km. The intercept (c) of the regression line was equivalent to z_0 which is theoretically the height where the current velocity becomes zero.

The bottom stress (τ) was related to the near-bed density (φ) of the currents and shear velocity (u*) as $\tau = \varphi\, u^{*2}$ [14]. For each bed type, the shear velocities were calculated for all the velocity profiles at the data collection stations along the channel. The resulted bed shear stresses were then averaged at each location and normalized by the inlet velocity (u_{in}) and initial density (φ_{in}) as $\tau_{in} = \varphi_{in}\, u_{in}{}^2$, as illustrated in Figure 9. Additionally, the distance (X) of data collection stations from the inlet gate was normalized by the total

length L of the channel downstream of the gate. As seen, the shear stress was almost constant along the channel, which agrees with the findings of Nourmohammadi et al. [13]. However, the bottom stresses for the currents over the rough beds varied among the roughness configurations.

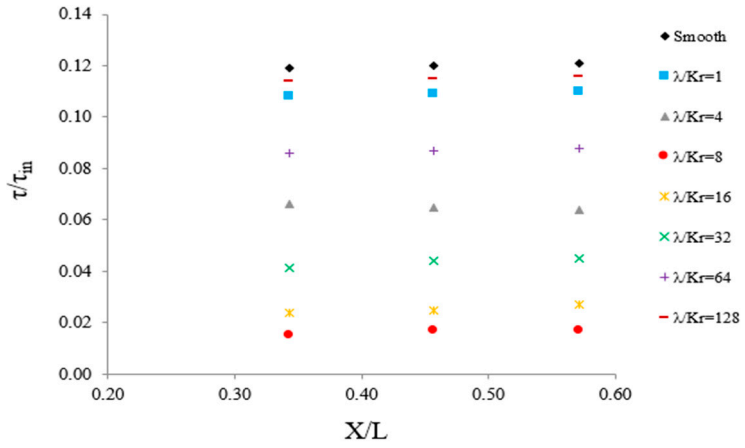

Figure 9. Bottom shear stress for different bed configurations.

For the λ/Kr = 1, the bottom stresses remained almost unchanged and similar to the case of the smooth bed. This can be attributed to the flow of these currents from above the elements in the case of this bed type, which minimizes the interaction of these currents with the bottom roughness. With increasing the gaps between the elements, the bottom stress levels decreased until the spacing of λ/Kr = 8 where its minimum occurred. This can be deduced that higher maximum velocity positions for these currents resulted in the reduction of bottom stresses. For the spacing above the critical one (roughened beds with λ/Kr = 16, 32, 64, 128), increasing the cavities between the beams rose the bottom shear stress. The bottom stresses for the currents over λ/Kr = 128 resembled those of the plane surface and remained roughly unchanged along the channel.

The shear stress at the bottom of a density current can induce bed erosion. The erosion of a soft mobile bed occurs when the bottom shear stress exerted by the density current exceeds the particle's threshold of motion [44]. The eroded sediments are entrained into the density currents creating self-sustaining currents which are highly unpredictable and destructive for marine engineering installations. These currents can maintain their forward motion for long distances if there is sufficient sediment exchange with the bed. According to the results, this can be implied that the existence of roughness arrays could inhibit erosion through decreasing bottom shear stress. Roughness-induced changes in the bed erosion-siltation balance could deteriorate the capacity of these currents to preserve their density and hence driving buoyancy forces.

3.4. Dimensional Analysis for Velocity Estimation

Dimensional analysis using Buckingham Pi theorem showed that the velocity of the currents was a function of Froude number (Fr_{in}), bed slope (S), and roughness parameter (λ/Kr) as:

$$\frac{\bar{u}}{u_{in}} = f(Fr_{in}, S, \frac{\lambda}{K_r}) \quad (7)$$

where $\bar{u}$ is the average velocity of the current and u_{in} is the velocity of the current at the inlet. Note that the Reynolds numbers at the inlet were almost more than 2000 for all the experiments and the currents were turbulent. Hence, the viscous effects could be neglected [39], and the Reynolds number was excluded from the analysis. The relationships between the dependent and independent parameters were determined by performing a regression analysis on the experimental data using the statistical package SPSS. Sixty

percent of the experimental data were used for the regression analysis. The coefficient of determination (R^2) was used here to display how well our datasets fit the proposed relations. To verify the accuracy of the proposed relations, the amount of error (E) was calculated. Forty percent of the datasets were used herein to investigate the accuracy of the driven equations. The error measures differences between values predicted by the equations and the observed values from the experimentation as $E = \frac{\sum_{i=1}^{n}|u_O - u_P|}{\sum_{i=1}^{n} u_O}$, where u_O is the velocities driven from the observed data at the experiments, u_P is the velocities predicted by the proposed relationships, and n is the number of velocities. For the smooth bed, the following equation was drawn:

$$\frac{\overline{u}}{u_{in}} = 2.263\ (Fr_{in})^{0.245}\ S^{0.026} \quad R2\ = 0.80,\ E = 10.3\% \tag{8}$$

With including the roughness parameter, the relationships for the roughened beds with $1 < \lambda/Kr \leq 8$ and $8 < \lambda/Kr \leq 128$ are shown in Equations (9) and (10), respectively.

$$\frac{\overline{u}}{u_{in}} = 2.250\ (Fr_{in})^{0.245}\left(\frac{\lambda}{K_r}\right)^{-0.128} S^{0.026} \quad R2\ = 0.81,\ E = 11.6\% \tag{9}$$

$$\frac{\overline{u}}{u_{in}} = 1.452\ (Fr_{in})^{0.245}\left(\frac{\lambda}{K_r}\right)^{0.085} S^{0.026} \quad R2\ = 0.80,\ E = 11.1\% \tag{10}$$

Herein, the values of the coefficient of determination were close to unity showing our data fit the suggested relationships well. The errors were also near zero indicating minimal differences between the values predicted by the suggested relationships and the ones measured in the laboratory. As mentioned before, forty percent of the dataset was used for error analysis of the proposed equations. To illustrate the accuracy of the equations, the measured values of mean velocities for this dataset were drawn against their predicted values by the equations, as seen in Figure 10. This demonstrates that the suggested relationships could estimate the mean velocities almost within the range of ±15% error.

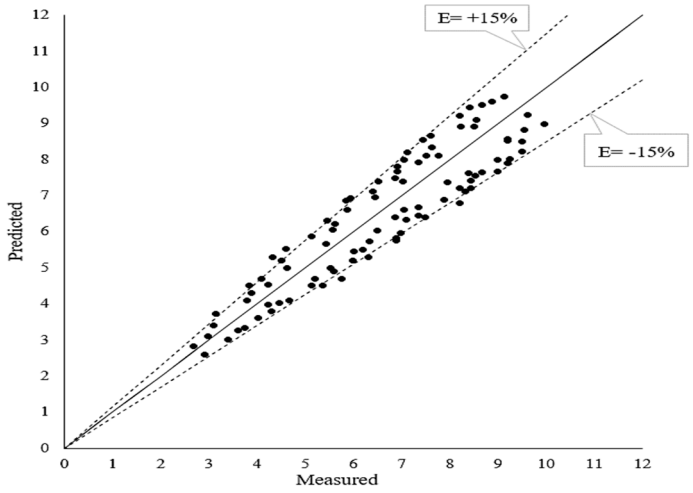

Figure 10. Comparison of the measured and predicted values of the mean velocities (cm/s).

4. Conclusions

This study aimed to explain the velocity structure of density currents over rough beds. The coefficients of the well-known relationships for wall and jet regions of the velocity profiles were modified for different bed roughness configurations. While the bed roughness was found to notably affect the shape of velocity profiles in the inner region, the alterations in the outer regions were minimal. The primary influence of roughness was decreasing the

velocity of density currents. However, the magnitude of this deceleration depended on the spacing of the roughness elements. For the rough bed with $\lambda/Kr = 1$, the velocity profiles resembled those of the smooth surface and markedly differed from other roughened cases. There was also a critical spacing of the roughness elements ($\lambda/Kr = 8$) over which the currents demonstrated the lowest velocities and the highest location of peak velocities. For the spacing more than the critical value, the influence of bottom roughness was diminished. In other words, increasing the distance between elements had little impact on reducing the velocity of the currents. The rough bed with $\lambda/Kr = 128$ demonstrated very little influence on the currents, and the flow dynamics reverted to that of the smooth bed.

Based on the dimensional analysis, new equations were developed in which the average velocity of the currents was related to inlet Froude number, bed roughness, and bed slope. It was also observed that roughness-induced changes in the velocity of currents can alter shear stress along the bed. The bottom stresses declined as the gaps between the elements increased and reached their minimum at the spacing of $\lambda/Kr = 8$. In dam reservoirs, the deceleration of currents allows more time for sedimentation, and this decreases the sediment concentration which is their driving force. Additionally, roughness-induced changes in the velocity profiles inhibit erosion by decreasing the bed shear stress. Therefore, bed roughness can be effective in the control of density-driven currents in the reservoirs and can prolong their lifespan.

Author Contributions: Conceptualization, R.N. and M.H.J.; data curation, R.N. and M.H.J.; formal analysis, R.N. and M.H.J.; funding acquisition, R.N., M.H.J., Z.I. (Zulhilmi Ismail), Z.I. (Zulkiflee Ibrahim), M.J., M.R.M.H. and D.S.M.I.; investigation, R.N. and M.H.J.; methodology, R.N. and M.H.J.; project administration, R.N. and M.H.J.; resources, R.N., M.H.J. and Z.I. (Zulhilmi Ismail); software, R.N.; supervision, M.H.J. and Z.I. (Zulhilmi Ismail); validation, R.N., M.H.J. and Z.I. (Zulhilmi Ismail); visualization, R.N.; writing—original draft, R.N. and M.H.J.; writing—review and editing, R.N., M.H.J., Z.I. (Zulhilmi Ismail), Z.I. (Zulkiflee Ibrahim), M.J., M.R.M.H. and D.S.M.I. All authors have read and agreed to the published version of the manuscript.

Funding: The funding for this study was provided by the Fundamental Research Grant Scheme (FRGS/1/2015/STWN01/UTM/02/2) under the Ministry of Higher Education Malaysia, and Research University Grant (Q.J130000.2522.09H06) by Universiti Teknologi Malaysia. The authors would also like to acknowledge the financial support under contract research from Bahtera Offshore (M) Sdn. Bhd. (R.J130000.7651.4C246).

Conflicts of Interest: The authors declare no conflict of interests.

References

1. Nogueira, H.I.; Adduce, C.; Alves, E.; Franca, M.J. Dynamics of the head of gravity currents. *Environ. Fluid Mech.* **2014**, *14*, 519–540. [CrossRef]
2. Tien, N.N.; Uu, D.V.; Cuong, D.H.; Mau, L.D.; Tung, N.X.; Hung, P.D. Mechanism of Formation and Estuarine Turbidity Maxima in the Hau River Mouth. *Water* **2020**, *12*, 2547. [CrossRef]
3. Wilson, R.I.; Friedrich, H. Coupling of Ultrasonic and Photometric Techniques for Synchronous Measurements of Unconfined Turbidity Currents. *Water* **2018**, *10*, 1246. [CrossRef]
4. Chamoun, S.; De Cesare, G.; Schleiss, A.J. Venting of turbidity currents approaching a rectangular opening on a horizontal bed. *J. Hydraul. Res.* **2017**, *56*, 44–58. [CrossRef]
5. Kostic, S.; Parker, G. Progradational sand-mud deltas in lakes and reservoirs. Part 1. Theory and numerical modeling. *J. Hydraul. Res.* **2003**, *41*, 127–140. [CrossRef]
6. Guo, Y.; Wu, X.; Pan, C.; Zhang, J. Numerical simulation of the tidal flow and suspended sediment transport in the Qiantang Estuary. *J. Waterw. Port Coast. Ocean Eng.* **2011**, *138*, 192–202. [CrossRef]
7. Xiao, Y.; Yang, F.; Zhou, Y.; Chen, W. 1-D numerical modeling of the mechanics of gravity-driven transport of fine sediments in the Three Gorges Reservoir. *Lake Reserv. Manag.* **2015**, *31*, 83–91. [CrossRef]
8. Wildt, D.; Hauer, C.; Habersack, H.; Tritthart, M. CFD Modelling of Particle-Driven Gravity Currents in Reservoirs. *Water* **2020**, *12*, 1403. [CrossRef]
9. Yoon, J.-I.; Sung, J.; Ho Lee, M. Velocity profiles and friction coefficients in circular open channels. *J. Hydraul. Res.* **2012**, *50*, 304–311. [CrossRef]

10. Cantero-Chinchilla, F.N.; Dey, S.; Castro-Orgaz, O.; Ali, S.Z. Hydrodynamic analysis of fully developed turbidity currents over plane beds based on self-preserving velocity and concentration distributions. *J. Geophys. Res. Earth Surf.* **2015**, *120*, 2176–2199. [CrossRef]
11. Firoozabadi, B.; Afshin, H.; Aram, E. Three-dimensional modeling of density current in a straight channel. *J. Hydraul. Eng.* **2009**, *135*, 393–402. [CrossRef]
12. Islam, M.A.; Imran, J. Vertical structure of continuous release saline and turbidity currents. *J. Geophys. Res. Ocean.* **2010**, 115. [CrossRef]
13. Nourmohammadi, Z.; Afshin, H.; Firoozabadi, B. Experimental observation of the flow structure of turbidity currents. *J. Hydraul. Res.* **2011**, *49*, 168–177. [CrossRef]
14. Cossu, R.; Wells, M.G. A comparison of the shear stress distribution in the bottom boundary layer of experimental density and turbidity currents. *Eur. J. Mech. B/Fluids* **2012**, *32*, 70–79. [CrossRef]
15. Cortés, A.; Rueda, F.; Wells, M. Experimental observations of the splitting of a gravity current at a density step in a stratified water body. *J. Geophys. Res. Ocean.* **2014**, *119*, 1038–1053. [CrossRef]
16. Chamoun, S.; De Cesare, G.; Schleiss, A.J. Influence of operational timing on the efficiency of venting turbidity currents. *J. Hydraul. Eng.* **2018**, *144*, 04018062. [CrossRef]
17. Oehy, C.D.; Schleiss, A.J. Control of turbidity currents in reservoirs by solid and permeable obstacles. *J. Hydraul. Eng.* **2007**, *133*, 637–648. [CrossRef]
18. Oshaghi, M.R.; Afshin, H.; Firoozabadi, B. Experimental investigation of the effect of obstacles on the behavior of turbidity currents. *Can. J. Civ. Eng.* **2013**, *40*, 343–352. [CrossRef]
19. Yaghoubi, S.; Afshin, H.; Firoozabadi, B.; Farizan, A. Experimental Investigation of the Effect of Inlet Concentration on the Behavior of Turbidity Currents in the Presence of Two Consecutive Obstacles. *J. Waterw. Port Coast. Ocean Eng.* **2017**, *143*, 04016018. [CrossRef]
20. Goodarzi, D.; Lari, K.S.; Khavasi, E.; Abolfathi, S. Large eddy simulation of turbidity currents in a narrow channel with different obstacle configurations. *Sci. Rep.* **2020**, *10*, 1–16. [CrossRef]
21. Negretti, M.E.; Zhu, D.Z.; Jirka, G.H. The effect of bottom roughness in two-layer flows down a slope. *Dyn. Atmos. Ocean.* **2008**, *45*, 46–68. [CrossRef]
22. Peters, W.D. Rough-Surface Gravity Current Flows. Ph.D. Thesis, Department of Mechanical Engineering, University of New Brunswick, Saint John, NB, Canada, 1999.
23. Tanino, Y.; Nepf, H.; Kulis, P. Gravity currents in aquatic canopies. *Water Resour. Res.* **2005**, 41. [CrossRef]
24. Tokyay, T.E. *A Les Study on Gravity Currents Propagating over Roughness Elements*; University of Lowa: Iowa City, IA, USA, 2010.
25. Chowdhury, R.A. Effect of Roughness on Density Currents. Master's Thesis, The University of Texas, San Antonio, TX, USA, 2013.
26. Bhaganagar, K. Direct numerical simulation of lock-exchange density currents over the rough wall in slumping phase. *J. Hydraul. Res.* **2014**, *52*, 386–398. [CrossRef]
27. Howlett, D.M.; Ge, Z.; Nemec, W.; Gawthorpe, R.L.; Rotevatn, A.; Jackson, C.A.L. Response of unconfined turbidity current to deep-water fold and thrust belt topography: Orthogonal incidence on solitary and segmented folds. *Sedimentology* **2019**, *66*, 2425–2454. [CrossRef]
28. Nasrollahpour, R.; Jamal, M.H.; Ismail, Z.; Rusli, N.M. Experiments on the dynamics of density currents. *J. Teknol.* **2016**, *78*, 71–76. [CrossRef]
29. Köllner, T.; Meredith, A.; Nokes, R.; Meiburg, E. Gravity currents over fixed beds of monodisperse spheres. *J. Fluid Mech.* **2020**, 901. [CrossRef]
30. Blanchette, F.; Strauss, M.; Meiburg, E.; Kneller, B.; Glinsky, M.E. High-resolution numerical simulations of resuspending gravity currents: Conditions for self-sustainment. *J. Geophys. Res. Ocean.* **2005**, 110. [CrossRef]
31. Perez-Gruszkiewicz, S.E. Reducing underwater-slide impact forces on pipelines by streamlining. *J. Waterw. Port Coast. Ocean Eng.* **2011**, *138*, 142–148. [CrossRef]
32. Lintern, D.G.; Hill, P.R.; Stacey, C. Powerful unconfined turbidity current captured by cabled observatory on the Fraser River delta slope, British Columbia, Canada. *Sedimentology* **2016**, *63*, 1041–1064. [CrossRef]
33. Nortek. *Comprehensive Manual*; Nortek: Providence, RI, USA, 2013.
34. Batt, R.L. *The Influence of Bed Roughness on the Dynamics of Gravity Currents*; University of Leeds: Leeds, UK, 2008.
35. Perry, A.E.; Schofield, W.H.; Joubert, P.N. Rough wall turbulent boundary layers. *J. Fluid Mech.* **1969**, *37*, 383–413. [CrossRef]
36. Khavasi, E.; Afshin, H.; Firoozabadi, B. Effect of selected parameters on the depositional behaviour of turbidity currents. *J. Hydraul. Res.* **2012**, *50*, 60–69. [CrossRef]
37. Ellison, T.; Turner, J. Turbulent entrainment in stratified flows. *J. Fluid Mech.* **1959**, *6*, 423–448. [CrossRef]
38. Altinakar, M.; Graf, W.; Hopfinger, E. Flow structure in turbidity currents. *J. Hydraul. Res.* **1996**, *34*, 713–718. [CrossRef]
39. He, Z.; Zhao, L.; Lin, T.; Hu, P.; Lv, Y.; Ho, H.-C.; Lin, Y.-T. Hydrodynamics of Gravity Currents Down a Ramp in Linearly Stratified Environments. *J. Hydraul. Eng.* **2017**, *143*, 04016085. [CrossRef]
40. Peters, W.D.; Venart, J. Visualization of rough-surface gravity current flows using laser-induced fluorescence. In Proceedings of the 9th International Symposium of Flow Visualization, Edinburgh, UK, 22–25 August 2000.
41. Leonardi, S.; Orlandi, P.; Smalley, R.; Djenidi, L.; Antonia, R. Direct numerical simulations of turbulent channel flow with transverse square bars on one wall. *J. Fluid Mech.* **2003**, *491*, 229–238. [CrossRef]

42. Leonardi, S.; Orlandi, P.; Djenidi, L.; Antonia, R. Structure of turbulent channel flow with square bars on one wall. *Int. J. Heat Fluid Flow* **2004**, *25*, 384–392. [CrossRef]
43. Dallimore, C.J.; Imberger, J.; Ishikawa, T. Entrainment and turbulence in saline underflow in Lake Ogawara. *J. Hydraul. Eng.* **2001**, *127*, 937–948. [CrossRef]
44. Hsu, S.M.; Tseng, C.M.; Lin, C.C. Antecedent Bottom Conditions of Reservoirs as Key Factors for High Turbidity in Muddy Water Caused by Storm Rainfall. *J. Hydraul. Eng.* **2017**, *143*, 05016006. [CrossRef]